nature research

https://doi.org/10.1038/s41566-020-00702-w

Supplementary information

Transient optical symmetry breaking for ultrafast broadband dichroism in plasmonic metasurfaces

In the format provided by the authors and unedited

Supplementary Information for: Transient optical symmetry breaking for ultrafast broadband dichroism in plasmonic metasurfaces

Andrea Schirato[1,5⋆], Margherita Maiuri[1,2⋆], Andrea Toma[5], Silvio Fugattini[5], Remo Proietti Zaccaria[5,6], Paolo Laporta[1,2], Peter Nordlander[3,4], Giulio Cerullo[1,2], Alessandro Alabastri[3⊗], and Giuseppe Della Valle[1,2⊗]

[1] *Dipartimento di Fisica - Politecnico di Milano, Piazza Leonardo da Vinci, 32, I-20133 Milano, Italy,*
[2] *Istituto di Fotonica e Nanotecnologie - Consiglio Nazionale delle Ricerche, Piazza Leonardo da Vinci, 32, I-20133 Milano, Italy,*
[3] *Department of Electrical and Computer Engineering, Rice University, 6100 Main Street, Houston, TX 77005,*
[4] *Department of Physics and Astronomy, Laboratory for Nanophotonics, Rice University, 6100 Main Street, Houston, TX 77005,*
[5] *Istituto Italiano di Tecnologia, via Morego 30, I-16163, Genova, Italy,*
[6] *Cixi Institute of Biomedical Engineering, Ningbo Institute of Industrial Technology, Chinese Academy of Sciences, 1219 Zhongguan West Road, Ningbo 315201, China*

I. STATIC RESPONSE

First of all, polarisation-resolved linear extinction measurements have been performed to ascertain the isotropic optical response of the fabricated square array of gold nanocrosses. The measured transmission spectrum of the sample in the experimentally available wavelength range (∼530-980 nm) is shown in Fig. S1a. These data have been exploited to refine the electromagnetic FEM analysis of the structure.

We assumed an ideal configuration made of an infinite 2D array of the square unit cell reported in Fig. 1c (see main text). The geometrical parameters (cf. main text of the paper) have been finely adjusted within the uncertainty range estimated by SEM images of the sample (Fig. 1a), in order to achieve a best fit with the static measurements of Fig. S1a. The results of our simulations are shown in Fig. S1b.

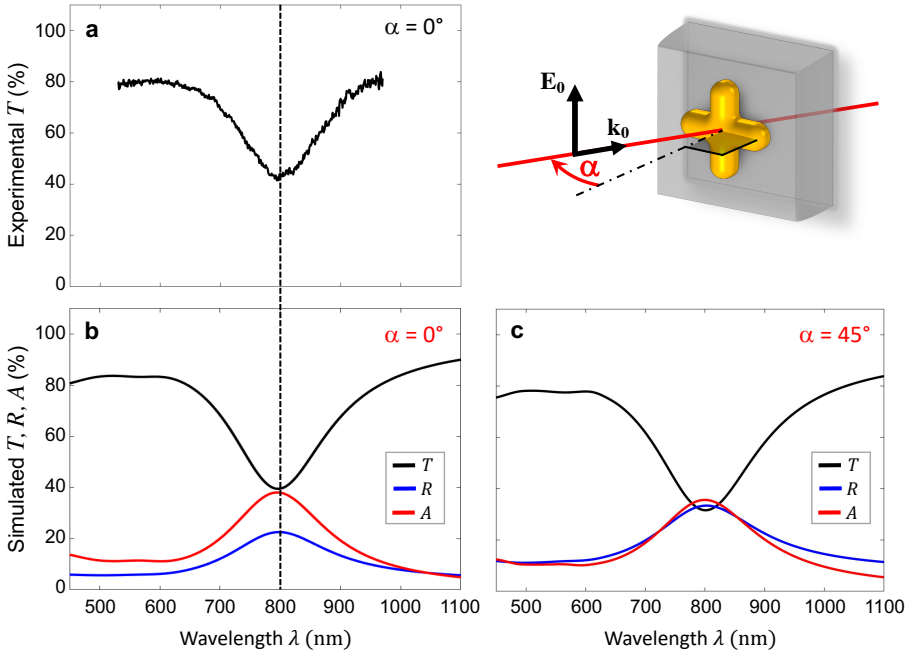

FIG. S1. **Static optical response of the nanocross metasurface.** **a**, Measured transmission spectrum of the fabricated sample. **b**, Simulated optical response of the unperturbed Au nanocross metasurface. Note that the plasmonic resonance of the structure dominates its transmission (black), reflection (blue) and absorption (red) spectra. **c**, Same as (b) with an incidence angle of $\alpha = 45°$, with α defined as in the upper inset sketch.

Note the good agreement between experimental and simulated transmission (black curves in Figs. S1a and S1b, respectively), especially in terms of the spectral position and width of the plasmonic resonance dip. In particular, a slight blue-shift of less than 5 nm is retrieved in the simulations for optimized values of the geometrical parameters. This shift explains the choice of slightly different wavelengths for the cross-sections of Figs. 4c-4d.

Note additionally that a quantitative agreement is also achieved in terms of the depth of the transmission dip, even though the simulations retrieve a 5% higher extinction at resonance.

Furthermore, the dependence of the metasurface optical response on the angle of incidence of the illuminating beam has been theoretically investigated. As depicted in the scheme (inset) of Fig. S1, we varied the angle α between the incident wave vector $\vec{k}_0$ and the normal to the metasurface plane, while keeping the same polarisation (i.e. electric field aligned with one arm of the nanocross). Angles up to 45°, as shown in Fig. S1c, have been tested. For increasing angles of incidence, an increase in reflectance is observed while transmittance decreases, resulting in a slight modification of the system absorption curve if compared to the case at normal incidence (cf. Fig. S1b). Nevertheless, the same clear resonant profile is observed, being due to the same plasmonic resonant mode excitation for a given polarisation. Importantly, the observed incidence angle insensitivity of the system provides the evidence that the optical response is dominated by the plasmonic features reminiscent of the single arm of the nanocross, and is only marginally modified by the excitation angle of incidence. This behaviour points in favour of a robustness of the symmetry-breaking mechanism exploited in our design, as detailed below (see Fig. S6).

II. THE HOMOGENEOUS 3TM

A. Time-domain evolution

Our model is a generalization of the homogeneous 3TM, proposed for the first time by Sun and co-workers [1], which describes the dynamics of the energy transfer following ultrafast photoexcitation in terms of the already mentioned three energetic degrees of freedom of the bulk material: the excess energy density stored in the whole population of nonthermal electrons (N), the electronic temperature of the thermal carriers (Θ_e) and the lattice temperature (Θ_l). In the 3TM no spatial dependence is considered and the model equations read as a set of coupled *ordinary* differential equations [1]:

$$\frac{\mathrm{d}N(t)}{\mathrm{d}t} = -aN(t) - bN(t) + P_{abs}(t), \tag{S1}$$

$$C_e \frac{\mathrm{d}\Theta_e(t)}{\mathrm{d}t} = -G\Big(\Theta_e(t) - \Theta_l(t)\Big) + aN(t), \tag{S2}$$

$$C_l \frac{\mathrm{d}\Theta_l(t)}{\mathrm{d}t} = G\Big(\Theta_e(t) - \Theta_l(t)\Big) + bN(t), \tag{S3}$$

where, formally, the energy density $N(t)$ is (linearly) related to the variation of occupation probability of electrons $\Delta f_{NT}(E,t)$ through an energy-dependent term $\delta_{NT}(E)$, representing the change in the electron energy distribution. Indeed, such $\delta_{NT}(E)$ accounts for the average spectral modification of the carrier distribution induced by a pump photon at a given energy, and can be written as a double-step-like function [2]. Importantly, the choice of such model as the basis of our I3TM prevented us from missing the description of a key contribution to the transient optical response on the considered, ultrashort, time scale, that is the population of nonthermal carriers, not comprised in the simpler Two-Temperature Model [3], which assumes an instantaneous thermalization of electrons.

Coefficients in Eqs. (S1)-(S3) essentially govern the energy transfer between the degrees of freedom involved in the relaxation following photoexcitation. Starting from a, this is the *electron gas heating rate*, determined as an average value over energies from a rigorous expression of the electron-electron scattering rate τ_{e-e} by comparison with more formal and fundamental calculations (the Extended Two-Temperature Model [2] or even the Boltzmann equation model [5, 6]). Indeed, according to Fermi liquid theory, the electron-electron scattering rate, showing a quadratic dependence on energy, can be written as [7]:

$$\tau_{e-e} = \tau_0 \Big(\frac{E_F}{E - E_F}\Big)^2, \tag{S4}$$

with E_F the Au Fermi energy and τ_0 a constant depending on the metal. Although Lindhard dielectric function calculations in the framework of Fermi liquid theory upon random phase approximation [5] provide a formal expression for such a parameter, experimental evidence [4, 8] shows that these calculations tend to underestimate the value of τ_0. Typical values fitted on pump-probe experimental data (from experiments with limited temporal resolution of few hundreds fs) are in the range of 5-7 fs. Then, as $1/\tau_{e-e}$ ranges between two extrema, 0 and $1/\tau_1 = (\hbar\omega)^2/\tau_0 E_F^2$, since the energy of nonthermal carriers is assumed to be comprised between $-\hbar\omega$ and $+\hbar\omega$ ($\hbar\omega$ being the pump photon energy) from the Fermi energy, a is set to be equal to the average value of the scattering rate $1/\tau_{e-e}$, i.e. $a = 1/(2\tau_1)$.

Concerning b, the rate of energy transfer from the out-of-equilibrium electronic population to phonons, its expression follows from a rigorous definition of the electron-phonon relaxation time given in [9] then reformulated as in [2] considering an excitation with pump photon energy $\hbar\omega$:

$$\tau_{e-ph} = \frac{E - E_F}{E_{ph}/\tau_f} = \tau_f \frac{\hbar\omega}{k_B \Theta_D}, \tag{S5}$$

with $E_{ph} = k_B\Theta_D$ the order of magnitude of the energy of the phonons emitted by nonthermal electrons, k_B the Boltzmann constant, Θ_D the Au Debye temperature and τ_f the quasi-particle free flight time. Then $b = 1/\tau_{e-ph}$.

Regarding coefficients governing the thermal electron dynamics, both the heat capacity $C_e = C_e(\Theta_e)$ and the thermal electron-phonon coupling $G = G(\Theta_e)$ have been modelled after Lin and co-workers' calculations [13], determining the total density of states of Au via Density Functional Theory including both conduction and valence electrons (which turn out to be crucial for relatively high Θ_e). In particular, we used the following expressions:

$$C_e(\Theta_e) = \frac{\partial\langle E\rangle}{\partial\Theta_e} = \int_{-\infty}^{\infty} \frac{\partial f(E, \mu(\Theta_e), \Theta_e)}{\partial\Theta_e} g(E) E \mathrm{d}E, \tag{S6}$$

where $g(E)$ stands for the metal density of states while $\mu(\Theta_e)$ is the metal chemical potential, $f(E, \mu(\Theta_e), \Theta_e)$ the Fermi-Dirac electronic distribution, and

$$G(\Theta_e) = \frac{\pi \hbar k_B \Lambda \langle \omega_{ph}^2 \rangle}{g(E_F)} \int_{-\infty}^{\infty} g^2(E) \left(- \frac{\partial f}{\partial E} \right) \mathrm{d}E, \tag{S7}$$

with Λ a dimensionless electron-phonon coupling factor specific for Au, $\langle \omega_{ph}^2 \rangle$ the average value of the square of the phonon frequency. Table S1 summarizes the parameters used in the 3TM.

Parameter	Value	Units	Ref.
E_F	7.17	eV	[10]
Θ_D	165	K	[11]
τ_f	13.824	fs	[10, 12]
C_l	$2.49 \cdot 10^6$	J m^{-3}K^{-1}	[14]
Λ	0.15		[13, 15]
$\Lambda \langle \omega_{ph}^2 \rangle$	23 ± 4	meV^2	[13, 16]
β_{e-ph}	$1.95 \cdot 10^{48}$	s^{-1}J^{-2}K^{-1}	[22]
B	180	GPa	[10]
λ_G	2.95		[10]

TABLE S1. Parameters of our implementation of the 3TM (which is at the basis of the I3TM used in this work).

B. Permittivity changes

Once the dynamics of the energetic degrees of freedom of the metallic structure upon ultrashort pulse illumination have been determined by solving the 3TM (or the I3TM), the corresponding photogenerated permittivity modulation has to be computed. With this purpose, intraband and interband contributions have to be properly described.

1. Intraband contribution

In the framework of the modelling approach pursued in this work, the intraband contribution, written as a Drude term, is considered to be modified by a variation of electronic and lattice temperatures via the Drude damping Γ and the plasma pulsation ω_p. In particular, regarding the former, accounting for any energy-loss process due to electron scattering, it has been written as the sum [10] of independent scattering event rates [6]: $\Gamma = \Gamma_{e-e} + \Gamma_{e-ph}$. In the framework of Landau's Fermi liquid theory for an electronic gas at temperature Θ_e, Ref. 17 formally derived the expression for the electron-electron scattering rate:

$$\Gamma_{e-e}(\hbar\omega, \Theta_e) = \frac{\left(k_B \Theta_e\right)^2}{\hbar^2 \omega_p} \left[1 + \left(\frac{\hbar\omega}{2\pi k_B \Theta_e} \right)^2 \right], \tag{S8}$$

with $\hbar\omega$ the absorbed photon energy, by considering Umklapp collisions only, as normal scattering processes are not effective in assisting absorption of photons by electrons [18]. The electron-phonon rate Γ_{e-ph} can instead be determined by evaluating the absorption coefficient of conduction electrons by means of the Fermi golden rule at the second order, considering the whole set of possible initial and final states as well as the virtual intermediate electronic

states. As in Ref. 6, upon parabolic conduction band approximation [30], for phonon energies essentially negligible if compared to photons energy, as for optical frequencies, and as long as $\Theta_l > \Theta_D$, one has [19]:

$$\Gamma_{e-ph}\big(\hbar\omega,\Theta_l,\Theta_e\big) = \gamma_{e-ph}\frac{\Theta_l}{\hbar\omega}\int_0^\infty \sqrt{E}\sqrt{E+\hbar\omega}f\big(E,\Theta_e\big)\Big[1-f\big(E+\hbar\omega,\Theta_e\big)\Big]\mathrm{d}E, \tag{S9}$$

with E the electron energy, $f(E,\Theta_e)$ the Fermi-Dirac occupation distribution and γ_{e-ph} a constant computed to match experimental data at room temperature. In this work we have set $\gamma_{e-ph} \approx 7\times10^{10}$ rad s^{-1}eV^{-1}K^{-1} to retrieve data from [20, 21]. For the limited range of electronic temperatures considered in our study, the electron-phonon scattering rate can be simplified as follows:

$$\Gamma_{e-ph}\big(\hbar\omega,\Theta_l\big) \simeq \Gamma^0_{e-ph}\big(\hbar\omega\big) + \beta_{e-ph}(\hbar\omega)^2\Delta\Theta_l, \tag{S10}$$

where Γ^0_{e-ph} is computed from Eq. (S9) by setting $\Theta_l = \Theta_e = \Theta_0 = 300$ K and $\beta_{e-ph} = 1.95\times10^{48}$ s^{-1}J^{-2}K^{-1} a linearisation constant in accord with Ref. 22.

Regarding the plasma pulsation contribution to intraband permittivity modulation, this streams from the volume expansion of the metallic structure, which in turns induces a variation in the free electron density within the Au conduction band. To determine its expression, one should consider the particle volume change with respect to its thermodynamic equilibrium value V_0, given by [23] $V(\Theta_e,\Theta_l) = V_0\big[1+\alpha(\Theta_e)\Delta\Theta_l\big]$, where the volume thermal expansion coefficient is [10, 24] $\alpha(\Theta_e) = \frac{1}{3B}\big[\lambda_G C_l + \frac{2}{3}C_e(\Theta_e)\big]$, with B the metal bulk modulus, λ_G the Grüneisen parameter. By comparing the total number of electrons in the conduction band, which is conserved although the temperature increases, one gets the expression we used to model the temperature dependence of the plasma angular frequency [25]:

$$\omega_p(\Theta_e,\Theta_l) = \sqrt{\frac{e^2}{\varepsilon_0 m^*}n(\Theta_e,\Theta_l)} = \frac{\omega_{p0}}{\sqrt{1+\alpha(\Theta_e)\Delta\Theta_l}}. \tag{S11}$$

with e the electron charge, ε_0 the vacuum permittivity, m^* the effective electron mass, n the conduction electron density and ω_{p0} the equilibrium value of the plasma frequency.

2. Interband contribution

Regarding interband (IB) modulation, driven by both N and Θ_e, variation of permittivity has been modelled starting from the analytical expression of ε_{IB} computed from the Au Joint Density of States (JDOS), i.e. the number of available direct transitions per unit volume between the valence and the conduction band, as proposed by Rosei and co-workers [26–30]. In these pioneering results, then extensively confirmed on both thin films [31] and nanoparticles [32, 33], Rosei reported a highly nonlinear thermo-modulation mechanism in metals and connected analytically the variation of energetic distribution of carriers due to absorption of radiation to the modification of optical transitions between valence (v) and conduction (c) bands. The main result of the investigations in Refs. 28–30 is therefore the expression of the imaginary interband permittivity (its real part being readily obtained via Kramers-Kronig relations), given by:

$$\varepsilon''_{IB}(\omega,\Theta_e) = \frac{\pi e^2|\vec{p}_{v,c}|^2}{3\varepsilon_0 m_e^2\omega^2}J_{v,c}(\omega,\Theta_e), \tag{S12}$$

upon constant matrix element approximation, where e is the electron charge, m_e its free mass, $\vec{p}_{v,c}$ the vectorial dipole matrix element between valence and conduction states of lattice vector $\vec{k}$ and $\hbar\omega$ the incoming photon energy. The JDOS, quantifying the number of existing couples of states within the entire first Brillouin Zone ($1BZ$) with energy separation equal to the pump pulse photon energy $\hbar\omega$ and therefore responsible for the interband absorption is analytically given by [34]:

$$J_{v,c}(\omega,\Theta_e) = \frac{2}{(2\pi)^3}\int_{1BZ} f[E_v(\vec{k}),\Theta_e]\big(1-f[E_c(\vec{k}),\Theta_e]\big)\delta\Big[E_c(\vec{k})-E_v(\vec{k})-\hbar\omega\Big]\mathrm{d}\vec{k}, \tag{S13}$$

where $E_{v/c}(\vec{k})$ stands for the valence/conduction band energy, $\delta(E)$ is the Dirac delta function and $f(E,\Theta_e)$ the Fermi-Dirac electronic distribution.

When conduction electrons are brought out of equilibrium by a photoinduced heating, the interband absorption is affected by the so-called *Fermi smearing* [30]: the electron distribution around the Fermi energy is smeared and the effective optical properties of the metal modified. Therefore, by starting from the expression of change in the occupation

probability due to the thermalised (T, via Θ_e) and the nonthermalised (NT, via N) fraction of electron population, $\Delta f_{T(NT)}$, one can evaluate the corresponding variation $\Delta J_{T(NT)}$ of the JDOS [34, 39]. The photoinduced variation of permittivity is then straightforwardly determined by exploiting Eq. (S12), and eventually $\Delta\varepsilon''_{IB} = \Delta\varepsilon''_{IB,T} + \Delta\varepsilon''_{IB,NT}$, each term having a peculiar spectral dispersion and structure modification as Θ_e and N vary, respectively. Their interplay results into a non-trivial dynamics following photoexcitation.

It is worth pointing out that in the framework of the I3TM here reported, all quantities mentioned above are defined locally and depend on space, since so do $N(\vec{r},t)$, $\Theta_e(\vec{r},t)$ and $\Theta_l(\vec{r},t)$, resulting into an inhomogeneous permittivity modulation evolving over time.

III. VALIDATION OF THE HOMOGENEOUS 3TM AND EXTENSION TO THE I3TM

A. Validation of the 3TM

To validate our modelling approach we started by comparing results obtained by our 3TM implementation with both theoretical and experimental results from specialised literature.

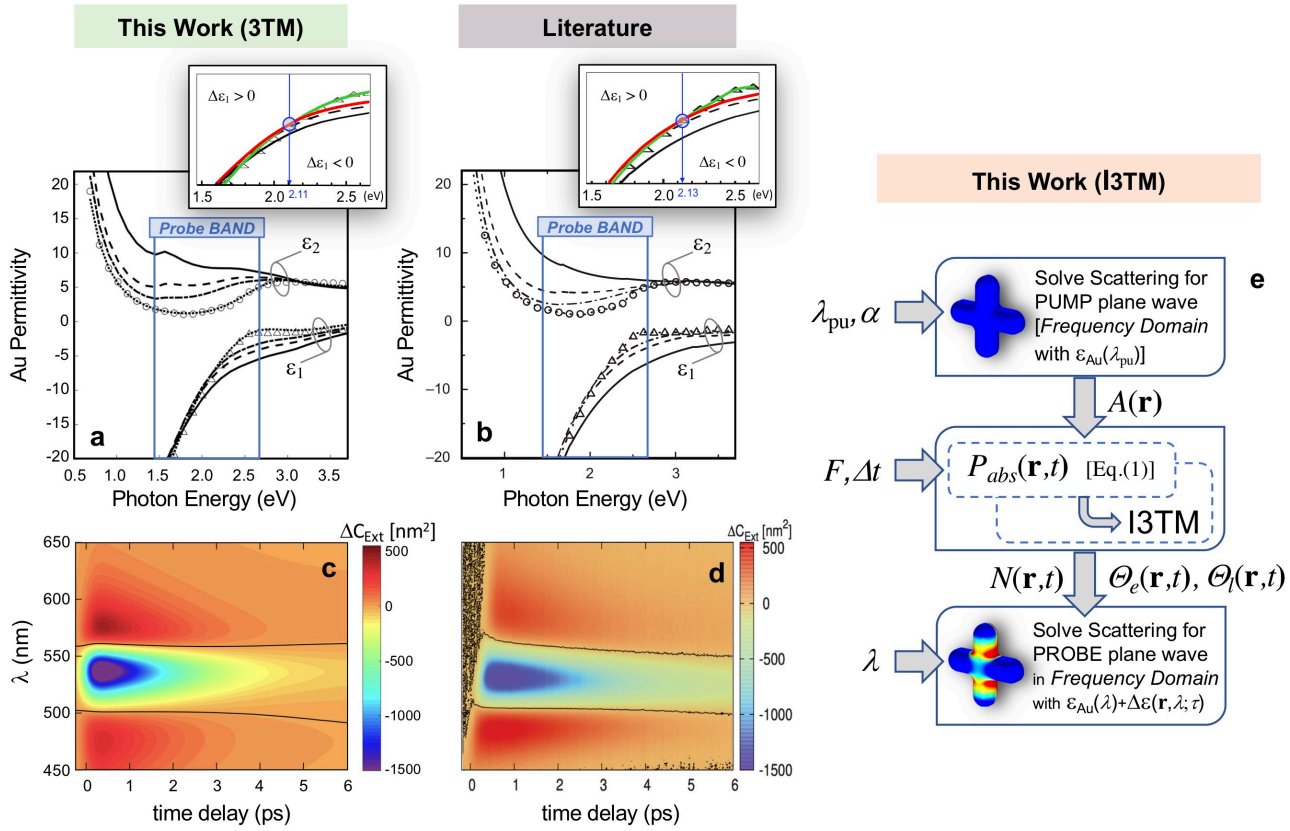

FIG. S2. **3TM validation and I3TM extension. a - b,** Results from our model (left) are compared with Ref. 35 [*Physics of Plasmas* **24**, 113106, 2017] (right), theoretically computing the real (ε_1) and imaginary (ε_2) parts of Au permittivity as a function of electronic and phononic temperatures. The spectra refer to $\Theta_e = \Theta_l = 300$ K (dotted lines); $\Theta_e = 3000$ K, $\Theta_l = 350$ K (dashed-dotted lines); $\Theta_e = 5000$ K, $\Theta_l = 370$ K (dashed lines); $\Theta_e = 10000$ K, $\Theta_l = 400$ K (solid lines). Experimental data from Johnson and Christy paper [20] are shown as well (open triangles for ε_1, open circles for ε_2). Insets of both panels focus on the real part in the probe band considered in this work, and compare the ε_1 spectrum at equilibrium (green lines) with the excited conditions $\Theta_e = 3000$ K, $\Theta_l = 350$ K, namely the closest to our experiments. The vertical blue line highlights the point of intersection of the curves, for which the variation $\Delta\varepsilon_1$ changes in sign. **c - d**, Dynamical broadband calculations obtained by our model (left) are compared with experimental results reported in Ref. 36 [*Phys. Rev. Lett.* **118**, 087401, 2017] (right), measuring the differential extinction cross section of photoexcited colloidal Au nanoparticles. **e**, Sketch of the algorithm for the implementation of the I3TM reported in this work. Input and output quantities of each computational step are pointed out. Adapted with permission from: (b) Ref. 35, Copyright 2017 AIP Publishing; (d) Ref. 36, Copyright 2017 American Physical Society.

In particular, we performed a comparison with theoretical calculations of the permittivity variations due to an increase of both electronic and phononic temperatures from Ref. 35.

Results, shown in Figs. S2a-2b, exhibit an excellent agreement between the two modelling approaches. Spectra of both real and imaginary parts of permittivity follow the same trend for increasing values of Θ_e and Θ_l, especially in the probe band considered in the main text of this work. By referring to the insets of Figs. S2a-2b, showing the detail of the permittivity real part for the static and excited conditions, we retrieve the zero in $\Delta\varepsilon_1$ at the same spectral position, and the variations in the sign of the permittivity that we computed are consistent with results from literature. A further validation of the 3TM is provided by comparing our theoretical calculations (in the quasi-static limit) with experimental results reported by Brown and co-workers in Ref. 36, where colloidal Au nanoparticles of 60 nm diameter are photoexcited by ultrashort pulses. Figures S2c-2d, showing the transient maps of dynamical extinction cross section variations, do confirm a very good agreement between our theoretical predictions and experiments (apart from a scaling factor of the order of 2 in terms of the estimated incident pump fluence). Such an agreement endorses the validity of our modelling approach, in addition to the set of successful comparisons between simulations and measurements already obtained in our previous works [4, 37, 39, 40]. Hence, after having properly validated the 3TM, we went further to include spatial effects and formulated the inhomogeneous version of the 3TM - referred to as the I3TM - which is suited to reveal the photogenerated symmetry breaking at deep sub-wavelength scale.

B. Extension from the 3TM to the I3TM

Regarding the implementation of our I3TM, we followed the three-step conceptual scheme reported in Fig. S2e.

1. Pump-metasurface modal interaction in the linear regime

As detailed in the main text, the symmetry breaking effect observed in our nanocrosses metasurface is based on the modal interaction of the pump pulse with the nanostructure, giving rise to a highly inhomogeneous absorption pattern within the individual metaatom. For this reason, the description of such a nanoscale pattern is the starting point of our modelling. For a given pump photon energy or pump wavelength λ_{pu} and angle of incidence α, the pump-metaatom interaction is modelled with full-vectorial Maxwell's equations in frequency domain, by considering a monochromatic plane wave impinging on a Au nanocross at equilibrium conditions. The geometrical parameters used in the simulations ($L = 155$ nm, $W = 40$ nm, $H = 30$ nm, and 285 nm array period) were adapted from the nominal values (estimated from SEM analysis) in order to best fit the experimental transmission spectrum of the unperturbed structure (compare solid curve and dash-dotted curve in Fig. 1b). We also assumed smoothed edges of the nanocross with 20/8 nm radius of curvature for outer/inner corners. Port formalism in the frequency domain with periodic boundary conditions was adopted, so to simulate an infinite square array of nanocrosses, with plane wave excitation at normal incidence, linearly polarised along one of the nanocross arms (y-axis in Fig. 1c). The geometrical domains were finely meshed in order to resolve the effective (local) optical wavelength with at least 7 elements in the dielectric regions, whereas an even finer mesh was employed in gold (with linear element size comprised between 2.5 nm and 10 nm) so to correctly describe evanescent decay patterns in the nanocrosses.

Also, in order to mimic the broadening effects on the plasmonic resonance caused by large scale inhomogeneities (from one cell to the other of the metasurface) we modified the static value of the Drude damping to account for such a well-known effect on the spectral features of the optical response from experimental samples [40]. To do so, the analytical value of $\Gamma^0(\hbar\omega) = \Gamma_{e-e}(\hbar\omega, \Theta_e = \Theta_0, \Theta_l = \Theta_0) + \Gamma_{e-ph}(\hbar\omega, \Theta_e = \Theta_0, \Theta_l = \Theta_0)$ has been multiplied by a constant factor f_b, so that $\Gamma_b^0(\hbar\omega) = f_b\Gamma^0(\hbar\omega)$. To match static transmittance measurements (see Figs. S1a-1b), the value of f_b has been set to $f_b = 3$ for simulations. The resulting overall dynamical Drude damping becomes therefore $\Gamma_b(\hbar\omega, \Theta_e, \Theta_l) = f_b\Gamma^0(\hbar\omega) + \Delta\Gamma_{e-e}(\hbar\omega, \Theta_e, \Theta_l) + \Delta\Gamma_{e-ph}(\hbar\omega, \Theta_e, \Theta_l)$, where the dependence on electronic and lattice temperature is as described above.

Solution of Maxwell's equations in 3D provides the spatial pattern of $A(\vec{r})$ in each point of the structure.

2. Integration of the I3TM

From this information, and for the given pump pulse fluence F and time duration Δt (see main text), we defined the proper space and time dependent driving term $P_{abs}(\vec{r}, t)$ detailed in Eq. 5 to be used in our inhomogenous extension of the 3TM. Note that, formally, the formulation of the I3TM required the inclusion of electronic and phononic diffusion in Eqs. (S1)-(S3), resulting into Eqs. (2)-(4) of the main text. We thus introduced the Au lattice and electronic

thermal conductivities, κ_l and κ_e, respectively. The former has been considered as constant and its value, $\kappa_l = 317$ W m^{-1} K^{-1}, was taken after [14], whereas κ_e was taken in accord with Ref. 41, approximating the more fundamental expression from [10] and written as $\kappa_e = \kappa_l \Theta_e/\Theta_l$. Moreover, it is worth pointing out that, when moving from the 3TM to the I3TM, we doubled the value of the fitting parameter τ_0 (set to 13.5 fs) compared to the standard 3TM (5-7 fs), as it is well known that the latter underestimates the effective τ_{e-e}, compared to more refined models (see, e.g., Ref. 4). The partial differential equations of the I3TM are then integrated with the Generalised Alpha method, with a time step $dt = \Delta t/20$ (so to properly resolve the pump pulse driving the dynamics). With the solution $N(\vec{r}, t)$, $\Theta_e(\vec{r}, t)$ and $\Theta_l(\vec{r}, t)$ at hand, we then calculated the corresponding permittivity perturbation at time delay $t = \tau$ by following exactly the same approach described in section II.

3. *Probe scattering from the dynamical metasurface*

To model the interaction of the broadband probe pulse impinging on the structure at a time delay τ from the pump, we performed parametric frequency-domain simulations, solved for values of the wavelength λ spanning the probe spectrum and for a fixed pump-probe delay τ. At each time delay, the electromagnetic scattering problem is solved for Au nanocrosses having a modified permittivity, given by the sum of the static (and thus uniform) permittivity, $\varepsilon_{Au}(\lambda)$, and the pump-induced local permittivity modulation computed in the previous step at the considered time delay, $\Delta\varepsilon(\vec{r}, \lambda; \tau)$.

IV. CONTRIBUTIONS TO PERMITTIVITY MODULATION: DISENTANGLEMENT

The theoretically predicted Au permittivity modulation shows a non-trivial evolution in both time and space across the plasmonic nanocross throughout the observed ps-time range.

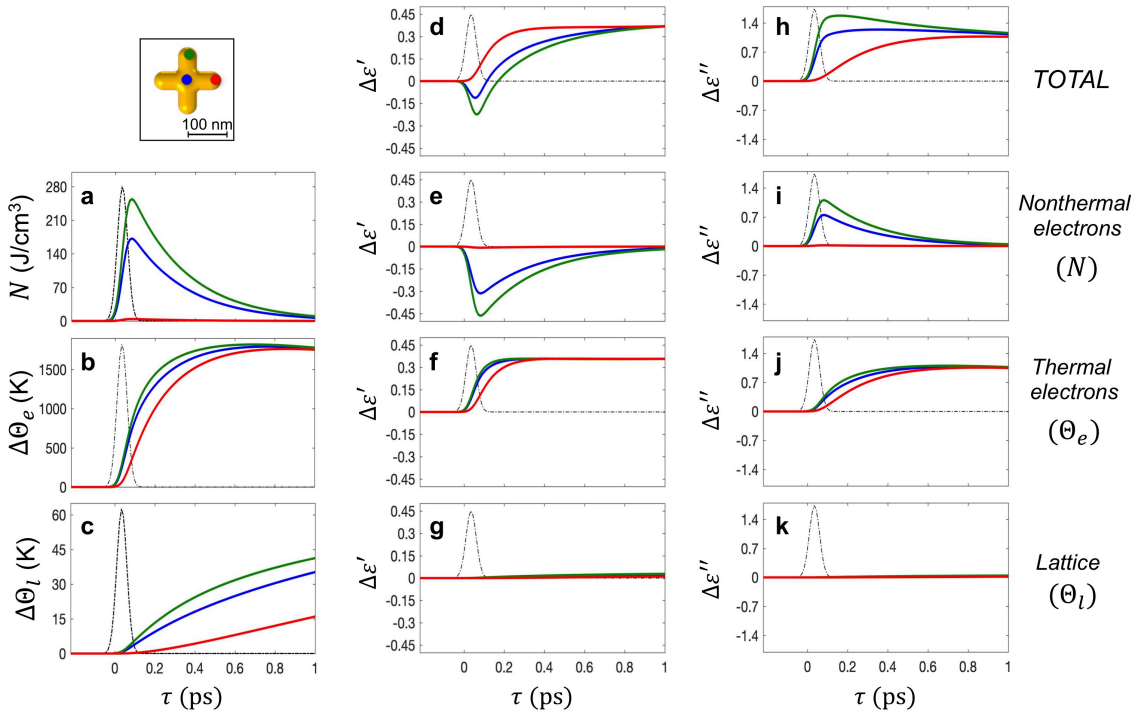

FIG. S3. **Disentangled contributions for permittivity variations. a - c**, From top to bottom: Time evolution of the plasmonic particle energetic degrees of freedom, i.e. energy density of nonthermal electrons $N(\vec{r}, t)$; electronic temperature $\Theta_e(\vec{r}, t)$; lattice temperature $\Theta_l(\vec{r}, t)$, shown for three exemplary points across the metaatom (refer to the upper left inset). **d - g**, From top to bottom: dynamics of the real part, $\Delta\varepsilon'$, of Au permittivity (here shown at 630 nm). The total modulation (d) is disentangled in its contributions, arising respectively from nonthermal carriers (e); thermalized electron gas (f); and the lattice temperature (g). **h - k**, Same as (d)-(g) for the permittivity imaginary part $\Delta\varepsilon''$. The dash-dotted line is the temporal profile of the pump pulse (refer to Methods for details).

Changes in sign, a highly dispersed behaviour and a non-homothetic evolution are observed. To understand how and to what extent the inner degrees of freedom solved for by the I3TM affect the single plasmonic metaatom permittivity, a complete disentanglement of all the contributions to permittivity modulation is provided. This has been done numerically by selectively activating the optical modifications arising from each one of the three internal degrees of freedom (N, Θ_e, Θ_l) leaving the other two at their equilibrium values. The results are shown in Fig. S3. For completeness, the time evolution of the corresponding degrees of freedom within the nanocross is shown as well (Figs. S3a-3c).

The comparison of the disentangled terms with the total $\Delta\varepsilon$ in three points of the structure (inset in Fig. S3) clearly shows that the permittivity modulation experienced by a probe pulse after a delay τ with respect to the pump results from a dynamical non-trivial interplay of all the contributions. At short pump-probe delays, modifications due to N give the most significant contribution and clearly drive the optical symmetry breaking. Interestingly, the disentanglement of the effects discloses the origin of the observed sign change in the permittivity real part for the wavelength here investigated (Fig. S3d). It indeed comes from the superposition of a negative contribution arising from nonthermal carriers (Fig. S3e) and a positive contribution due to thermal carriers (Fig. S3f). After few hundreds of fs though, effects from N start decreasing, and the electronic temperature Θ_e drives the optical modulation. Its contribution to the symmetry breaking is relevant on the time scale of electron thermal diffusion, after which the photoinduced symmetry breaking window closes. Finally, the contribution from the lattice temperature increase (Fig. S3c) is triggered at longer delays. Although Θ_l dynamics is activated even at short times (refer to Eq. (4) from the main text, which includes a term directly coupling phonons and the ultrafast nonthermal electronic population), its corresponding contribution to the optical perturbation (Figs. S3g and S3k) remains almost negligible within the considered ultrafast time scale.

V. SPACE-TIME DEPENDENT OPTICAL PERTURBATION

As mentioned in the main text, the numerical solution of the I3TM, describing the spatio-temporal dynamics of the internal energetic degrees of freedom of the plasmonic nanoparticles (see Eqs. (2)-(4) and Methods in the main text), is the starting point to compute the corresponding inhomogeneous optical perturbation.

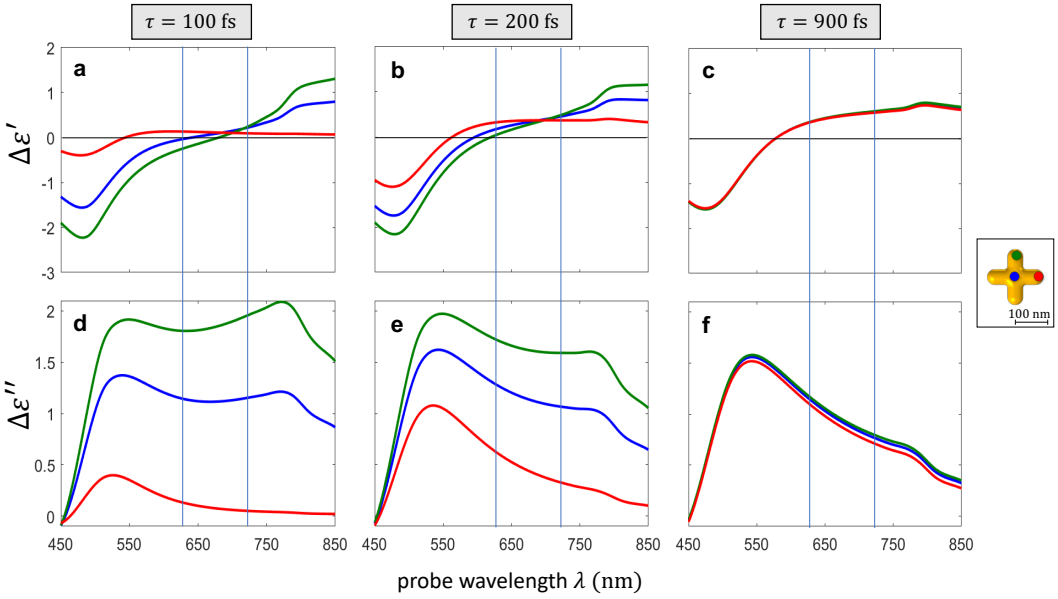

FIG. S4. **Space-time dependent dispersion of Au permittivity.** Numerically computed pump-induced nonlinear permittivity modulation spectra in different points of the Au nanocross and at different time delays. **a - c**, From left to right: spectra of the real part permittivity variation, $\Delta\varepsilon'(\vec{r},\lambda;\tau)$, at $\tau = 100$ fs, $\tau = 200$ fs, and $\tau = 900$ fs, respectively, evaluated at three characteristic positions visualized in the inset on the right. **d - f**, Same as (a)-(c) for the imaginary part permittivity variation $\Delta\varepsilon''(\vec{r},\lambda;\tau)$. Vertical lines in all panels highlight the two wavelengths more extensively discussed in the main text.

Such perturbation in the metallic nanocross, expressed in terms of the spectrally-dispersed complex-valued permittivity, $\varepsilon = \varepsilon(\vec{r},\lambda,t)$, is retrieved starting from the evolution of N, Θ_e and Θ_l according to the well-established nonlinearity model discussed above. Yet, the novelty introduced by the I3TM here reported is represented by the fact that, since

the rate equations (Eqs. 2-4) are solved locally, the permittivity modulation inherits both the spatial and the temporal dependences from the aforementioned energetic quantities and, as a three-dimensional non-uniform field, it follows a different dynamics in each point of the nanoparticle. Figure S4 highlights such aspects of the I3TM by showing the permittivity spectra, both in its real and imaginary parts, at different pump-probe time delays and in different points of the structure. A time evolution of the permittivity dispersion, non-trivially driven by the interplay of both the nonthermal and thermal hot carriers broadband contributions, is observed in each point of the nanoparticle. Interestingly, Figure S4 points out the fundamental origin of the ultrafast symmetry breaking that we here report. On a sub-picosecond time scale, the pump-driven optical perturbation exhibits an inhomogeneous pattern in space. Such non-uniform distribution for $\varepsilon(\vec{r}, \lambda, t)$ generates then the ultrafast polarisation-sensitive response theoretically predicted and experimentally observed. Indeed, the symmetry breaking temporal window, during which the spatial pattern of permittivity remains inhomogeneous, is mainly driven by the nonthermal carriers relaxation and the thermal hot carriers diffusion processes. The characteristic time scales of such energy dynamics, completed within a few hundreds of femtoseconds, entail the purely ultrafast nature of the dichroism we report. By exploiting these dynamics, the effect considered vanishes well before the complete return to thermodynamic equilibrium of the metaatoms.

Figures S4c and S4f provide a clear-cut evidence of this aspect: at a pump-probe delay of $\tau = 900$ fs the system is still strongly excited (the curves of $\Delta\varepsilon$ are definitely different from zero). However, at the same time delay homogenisation is achieved and optical symmetry restored (the curves referring to different positions fold and local inhomogeneities collapse), which closes the symmetry breaking window of the dichroic response.

Regarding sign and values of the predicted permittivity variations, the results here shown are consistent with literature results [37, 38].

VI. TRANSIENT TRANSMITTANCE

To complete and support data shown in the main text, where only differential transmittance data (either as a function of time or of wavelength) are shown (refer to Figs. 4a-4d), we here provide some spectra of the total transmittance at selected time delays, retrieved according to the following formula:

$$T_{\parallel,\perp}(\lambda,\tau) = \left[1 + \frac{\Delta T_{\parallel,\perp}(\lambda,\tau)}{T_0(\lambda)}\right] T_0(\lambda) = \left[1 + \Delta_{\parallel,\perp}(\lambda,\tau)\right] T_0(\lambda), \tag{S14}$$

where therefore $\Delta_{\parallel,\perp}(\lambda,\tau)$ is the dynamical measurement (as presented in Figs. 4c-4d), and $T_0(\lambda)$ is the static transmission spectrum (shown in Fig. S1a).

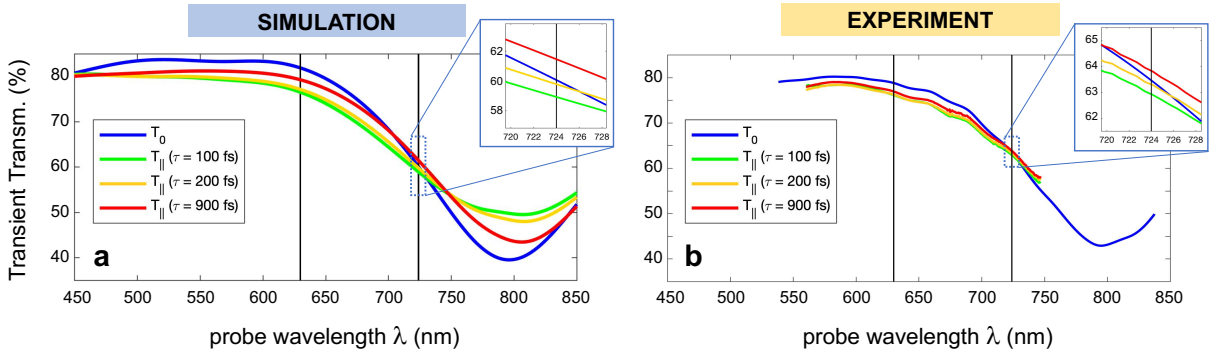

FIG. S5. **Transient transmittance.** Transmission spectra from **a**, simulations and **b**, experimental measurements, respectively, in static conditions (blue lines) and at $\tau = 100$ fs (green lines), $\tau = 200$ fs (yellow lines) and $\tau = 900$ fs (red lines) pump-probe delays for the probe polarization parallel to the pump one. Vertical lines highlight the wavelengths discussed in the main text, and the insets focus on the dynamical behaviour of transmittance in the vicinity of $\lambda = 724$ nm.

Results are shown in Fig. S5b and compared with theoretical predictions, in Fig. S5a, in the case of probe polarisation aligned with the pump polarisation, in the band experimentally available. To resolve the transmission dynamics, data from the static spectrum have been smoothed by applying a moving mean algorithm. The broadband measurement shows a complex dispersed behaviour of curves as a function of time delay. For wavelengths between 500 nm and 700 nm the dynamical transmission is always lower than the static case. As expected, this is indeed consistent with the negative signal shown in Figs. 4c-4d, upper traces. Moreover, such a negative variation of $T_{\parallel}(\lambda,\tau)$ in this spectral

region (i.e. far from the plasmonic resonance) is also consistent with the predicted variations of permittivity shown in Fig. S4. For optical wavelengths longer than 700 nm the dynamical behaviour is more complicated. The insets focusing at around 724 nm show that the optical transmission significantly decreases at very short delays (green line), then goes back close to the static curve (yellow line), and finally surpasses the static value for longer delays (red versus blue lines). This trend is consistent with what observed in the main text (Figs. 4c-4d).

Finally, note that simulated spectra of Figs. S4a-4d, enabling one to explore a broad range of wavelengths, provide us with a better insight on the global behaviour of the transient plasmonic resonance. At very short time delays, the transient transmittance is dominated by plasmonic resonance broadening, whereas at longer time delays, both broadening and red-shift take place.

VII. ROBUSTNESS OF THE SYMMETRY BREAKING

In discussing the polarisation-resolved pump-probe experimental set-up (see Methods in the main text), we pointed out that the pump beam was impinging at an angle $\alpha \sim 5°$ with respect to the normal direction. It is worth stressing that such an angle has no role in the phenomenon of photoinduced symmetry breaking for the metasurface under consideration. In fact, the broadband ultrafast dichroic response we predicted and observed in this work is rather linked to the modal interaction of the pump beam with the Au nanocrosses close to their plasmonic resonance, resulting in a highly inhomogeneous pattern of the photo-generated nonthermal carriers with deep subwavelength spatial gradients within the individual metaatoms.

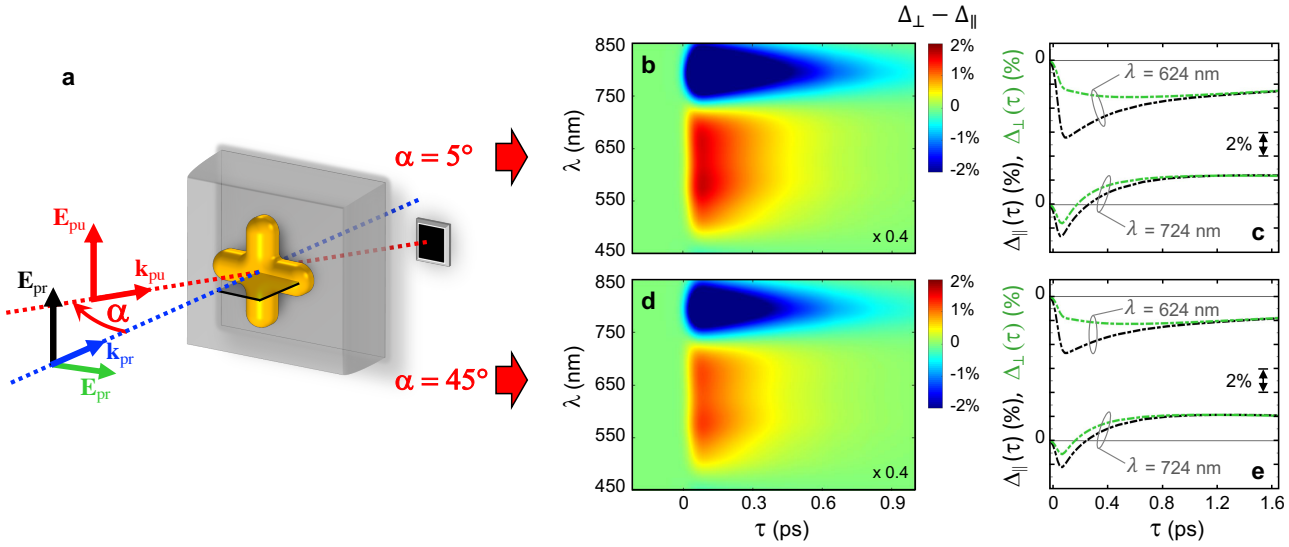

FIG. S6. **Robustness of the symmetry breaking.** Results from virtual pump-probe experiments where, as sketched in **a**, the pump pulse impinges with an angle α on the metasurface, while normal incidence is considered for the probe pulse. **b - c** From left to right: ultrafast dichroic spectrum $\Delta_\perp - \Delta_\parallel$ for different delays, and time evolution of the polarisation-resolved pump-probe traces $\Delta_{\parallel,\perp}$ (black and green, respectively) for an angle $\alpha = 5°$ between pump and probe wave vectors. **d - e** Same as (b)-(c) for $\alpha = 45°$.

In the case under consideration, such a modal pattern, determining the spatial distribution of the absorbed power density of the pump, is dominated by the plasmonic response reminiscent of the single nanocross arm aligned to the pump pulse polarisation and is unique for a fixed polarisation state. As a result, a change in the incidence angle, from $\alpha = 0°$ (as in the simulations shown in the main text) to $\alpha = 5°$ (as for the pump-probe measurements) only slightly affects the overall behaviour of the symmetric metasurface. To confirm the robustness of symmetry breaking with respect to the incidence angle, we performed numerical simulations for non-zero angle of incidence for the pump beam. As in the main text, the dichroic signal spectrum $\Delta_\perp - \Delta_\parallel$ is calculated for different time delays, and time sections of the two polarisation-resolved traces are also reported at two fixed exemplary wavelengths. A schematic representation of the set-up of the virtual pump-probe experiment is depicted in Fig. S6a, and simulation results are shown in Figs. S6b-6c for $\alpha = 5°$, and in Figs. S6d-6e for $\alpha = 45°$. Note that the results for low angles ($\alpha = 5°$) are almost identical to the case at normal incidence (cf. Figs. 3 and 4 in the main text). A noticeable variation in the dichroic signal does occur with $\alpha = 45°$, consistently with the variation of absorbed power for such a high incidence angle of the pump if compared to normal incidence conditions. Despite the quantitative decrease in absorbed power,

the absorption spatial pattern is *not* affected by α. On the contrary, it is determined by the pump polarisation state, which is kept fixed in our simulations. Our simulations confirm that the photoinduced symmetry breaking exploited in our design is a robust effect, governed by the spatial modal pattern of the plasmonic resonant mode at the pump wavelength, and being only marginally affected by the angle of incidence of the pump.

VIII. DOUBLE-PULSE MODULATION

The fact that the ultrafast symmetry breaking driving the broadband dichroism here reported is due to a hot carrier non-uniform spatial distribution implies that the phenomenon is fully reversible on a sub-ps time scale, limited by spatial diffusion instead of relaxation. For this reason, even when photoexcitation by ultrashort pulses at a repetition rate in the THz range is considered, the metasurface still exhibits the reported ultrafast modulation following interaction with each pulse. Although the metaatoms do not immediately relax back to the equilibrium state after a first pulse, their optical symmetry is recovered at ultrahigh speed, which makes them ready for another dichroic transition following a second pump pulse arriving at 1 ps time delay with respect to the first pulse.

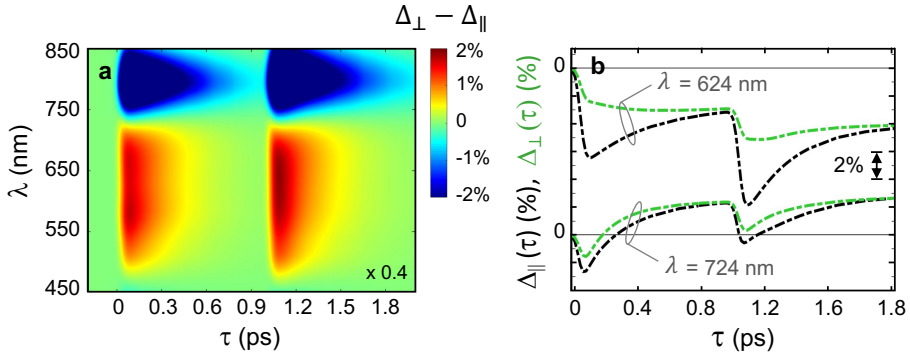

FIG. S7. **Double-pulse ultrafast dichroism.** Theoretical prediction of the ultrafast broadband dichroism $\Delta_\perp - \Delta_\parallel$ upon photoexcitation with *two* ultrashort pump pulses impinging on the plasmonic metasurface at a time delay of 1 ps from each other. **a**, Spectrum of the transient dichroism at different probe delays. **b**, Polarisation-resolved time evolution of $\Delta_{\parallel,\perp}$ (black and green, respectively) at two fixed wavelengths.

To ascertain such a capability, we simulated a virtual double-pulse pump-probe experiment. In particular, the I3TM (Eqs. 2-4) has been numerically solved for a source term describing two pulses exciting the metasurface with a relative 1 ps delay. Accordingly, Eq. 5 has been appropriately modified and written as follows:

$$P_{abs}(\vec{r},t) = \frac{FS}{V}\left[A_1(\vec{r})g_1(t) + A_2(\vec{r})g_2(t)\right], \tag{S15}$$

where F, S, V have the same meaning as in the main text, while $A_{1,2}(\vec{r})$ are the normalised spatial absorption patterns of the two pulses, respectively, and $g_{1,2}(t)$ are Gaussian intensity profiles of the pulses, time-shifted by $t_d = 1$ ps, namely $g_1(t) = \sqrt{4\ln 2/\pi\Delta t^2}\exp\{-4\ln 2(t-t_0)^2/\Delta t^2\}$ while $g_2(t) = \sqrt{4\ln 2/\pi\Delta t^2}\exp\{-4\ln 2[t-(t_0+t_d)]^2/\Delta t^2\}$. They share the same full width at half maximum in intensity $\Delta t = 60$ fs, but peaks are reached with a relative delay of t_d.

Concerning the absorption patterns, $A_1(\vec{r})$ is the same as in previous simulations, whereas $A_2(\vec{r})$ is computed in the same way but assuming a modified permittivity of gold $\varepsilon_{Au}(\vec{r},\lambda,\tau = t_0+t_d) = \varepsilon_{Au}^{static}(\lambda) + \Delta\varepsilon(\vec{r},\lambda,\tau = t_0+t_d)$, where $\Delta\varepsilon(\vec{r},\lambda,\tau = t_0+t_d)$ is the permittivity modulation evaluated at time delay t_0+t_d after the absorption of the first pump pulse. Results of simulations are shown in Fig. S7, in terms of dichroism $\Delta_\perp - \Delta_\parallel$ (Fig. S7a) and transient polarisation-resolved pump-probe traces (Fig. S7b). The results clearly show that the second pulse does not induce exactly the same transmission changes, consistently with the fact that it does not excite the system starting from the equilibrium condition, but rather from an excited yet isotropic state (refer to Figs. S4c,4f as well as Figs. 2a-2d for $\tau = 900$ fs). Nevertheless it is capable of breaking the isotropic configuration another time and produces, at time delays following $\tau = t_d$, a dichroic figure comparable to the one retrieved after the previous pump pulse.

[1] Sun, C.-K., Vallée, F., Acioli, L.H., Ippen, E.P. & Fujimoto, J.G. Femtosecond-tunable measurement of electron thermalization in gold. *Phys. Rev. B* **50**, 15337 (1994).

[2] Carpene, E. Ultrafast laser irradiation of metals: beyond the two-temperature model. *Phys. Rev. B* **74**, 024304 (2006).

[3] Anisimov, S.I., Kapeliovich, B.L. & Perel'man, T.L. Electron emission from metal surfaces exposed to ultrashort laser pulse. *Sov. Phys. JETP* **39**, 2, 375 (1974).

[4] Della Valle, G., Conforti, M., Longhi, S., Cerullo, G. & Brida, D. Real-time mapping of the dynamics of nonthermal electrons in thin gold film. *Phys. Rev. B* **86**, 155139 (2012).

[5] Fann, W.S., Storz, R., Tom, H.W.K. & Bokor, J. Electron thermalization in gold. *Phys. Rev. B* **46**, 13592 (1992).

[6] Labouret, T. & Palpant, B. Nonthermal model for ultrafast laser-induced plasma generation around a plasmonic nanorod. *Phys. Rev. B* **94**, 245426 (2016).

[7] Pines, D. & Nozières, P. *The Theory of Quantum Liquids* (Benjamin, New York, 1966).

[8] Besteiro, L.V., Kong, X.-T., Wang, Z., Hartland, G. & Govorov, A.O. Understanding hot-electron generation and plasmon relaxation in metal nanocrystals: quantum and classical mechanisms. *ACS Photon.* **4**, 2759 (2017).

[9] Groeneveld, R.H.M., Sprik, R. & Ladendjik, A. Femtosecond spectroscopy of electron-electron and electron-phonon energy relaxation in Ag and Au. *Phys. Rev. B* **51**, 11433 (1995).

[10] Ashcroft, N.W. & Mermin, N.D. *Solid State Physics* (Saunders College, Philadelphia, 1960).

[11] Kittel, C. *Introduction to Solid State Physics* (Wiley, New York, 1986).

[12] Halas, S. & Durakiewicz, T. Work functions of elements expressed in terms of the Fermi energy and the density of free electrons. *J. Phys.: Condens. Matter* **10**, 10815 (1998).

[13] Lin, Z., Zhigilei, L.V. & Celli, V. Electron-phonon coupling and electron heat capacity of metals under conditions of strong electron-phonon nonequilibrium. *Phys. Rev. B* **77**, 075133 (2008).

[14] Lide, D.R. *CRC Handbook of Chemistry and Physics* 74^{th} edn (CRC Press, Boca Raton, FL, 1993).

[15] Allen, P.B. Empirical electron-phonon λ values from resistivity of cubic metallic elements. *Phys. Rev. B* **36**, 2920 (1987).

[16] Brorson, S.D. et al. Femtosecond room-temperature measurement of the electron-phonon coupling constant λ in metallic superconductors. *Phys. Rev. Lett.* **64**, 2172 (1990).

[17] Gurzhi, R.N. Mutual electron correlations in metal optics. *Sov. Phys. JETP* **35**, 673-675 (1959).

[18] Ziman, J.M. *Electrons and Phonons* (Clarendon Press, Oxford, 1960).

[19] Tsai, C.Y. et al. Theoretical model for intravalley and intervalley free-carrier absorption in semiconductor lasers: beyond the classical Drude model. *IEEE J. Quant. Electron.* **34**, 3, 552-559 (1998).

[20] Johnson, P.B. & Christy, R.-W. Optical constants of the noble metals. *Phys. Rev. B* **6**, 4370 (1972).

[21] Etchegoin, P.G., Le Ru, E. & Meyer, M. An analytic model for the optical properties of gold. *J. Chem. Phys.* **125**, 164705 (2006).

[22] Smith, J.B. & Ehrenreich, H. Frequency dependence of the optical relaxation time in metals. *Phys. Rev. B* **25**, 923 (1982).

[23] Gurzhi, R.N. On the theory of the infrared absorptivity of metals. *Sov. Phys. JETP* **6**, 506 (1958).

[24] Crut, A., Maioli, P., Del Fatti, N. & Vallée, F. Acoustic vibrations of metal nano-objects: time-domain investigations. *Phys. Rep.* **549**, 1-43 (2015).

[25] Yeshchenko, O.A., Bondarchuk, I.S., Gurin, V.S., Dmitruk, I.M. & Kotko, A.V. Temperature dependence of the surface plasmon resonance in gold nanoparticles. *Surf. Sci.* **608**, 275 (2013).

[26] Rosei, R. & Lynch, D.W. Thermomodulation spectra of Al, Au, and Cu. *Phys. Rev. B* **5**, 3883 (1972).

[27] Rosei, R., Antonangeli, F. & Grassano, U.M. d bands position and width in gold from very low temperature thermomodulation measurements. *Surf. Sci.* **37**, 689-699 (1973).

[28] Rosei, R. Temperature modulation of the optical transitions involving the Fermi surface in Ag: theory. *Phys. Rev. B* **10**, 474-483 (1974).

[29] Rosei, R., Culp, C.H. & Weaver, J.H. Temperature modulation of the optical transitions involving the Fermi surface in Ag: experimental. *Phys. Rev. B* **10**, 484-489 (1974).

[30] Guerrisi, M., Rosei, R. & Winsemius, P. Splitting of the interband absorption edge in Au: temperature dependence. *Phys. Rev. B* **12**, 557 (1975).

[31] Hohlfeld, J. et al. Electron and lattice dynamics following optical excitation of metals. *Chem. Phys.* **251**, 237 (2000).

[32] Del Fatti, N. et al. Nonequilibrium electron dynamics in noble metals. *Phys. Rev. B* **61**, 16956 (2000).

[33] Baida, H. et al. Ultrafast nonlinear optical response of a single gold nanorod near its surface plasmon resonance. *Phys. Rev. Lett.* **107**, 057402 (2011).

[34] Marini, A. et al. Ultrafast nonlinear dynamics of surface plasmon polaritons in gold nanowires due to the intrinsic nonlinearity of metals. *New J. Phys.* **15**, 013033 (2013).

[35] Yurkevich, A.A., Ashitkov, S.I. & Agranat, M.B. Permittivity of gold with a strongly excited electronic subsystem. *Phys. Plasmas* **24**, 113106 (2017).

[36] Brown, A.M. et al. Experimental ab initio ultrafast carrier dynamics in plasmonic nanoparticles. *Phys. Rev. Lett.* **118**,

087401 (2017).
[37] Dal Conte, S. et al. Disentangling electrons and lattice nonlinear optical response in metal-dielectric Bragg filters. *Phys. Rev. B* **89**, 125122 (2014).
[38] Conforti, M. & Della Valle, G. Derivation of third-order nonlinear susceptibility of thin metal films as a delayed optical response. *Phys. Rev. B* **85**, 245423 (2012).
[39] Zavelani-Rossi, M. et al. Transient optical response of a single gold nanoantenna: the role of plasmon detuning. *ACS Photon.* **2** 521-529 (2015).
[40] Silva, M.G. et al. Universal saturation behavior in the transient optical response of plasmonic structures. *Phys. Rev. B* **98**, 115407 (2018).
[41] Kanavin, A.P. et al. Heat transport in metals irradiated by ultrashort laser pulses. *Phys. Rev. B* **57**, 698-703 (1998).